Delft University of Technology

MSc Thesis

Performed at:
Climate and Clouds
Faculty of Applied Sciences

Towards a physics-based understanding of fruit frost protection using wind machines

Candidate:
V. W. J. Heusinkveld

Supervisors:
Prof. dr. ir. B. J. H. van de Wiel
Ir. J. A. van Hooft

Graduation Committee:
Prof. dr. ir. B. J. H. van de Wiel
Prof. dr. A. P. Siebesma
Dr. ir. D. J. Verschuur
Dr. ir. M. C. ten Veldhuis
Ir. J. A. van Hooft

Delft
May 17, 2019

Towards a physics-based understanding of fruit frost protection using wind machines

Vincent W.J. Heusinkveld
Faculty of Civil Engineering and Geosciences, Department of Geoscience and Remote Sensing, Delft University of Technology, Delft, the Netherlands,
Vincent.Heusinkveld@Gmail.com

J. Antoon van Hooft
Faculty of Civil Engineering and Geosciences, Department of Geoscience and Remote Sensing, Delft University of Technology, Delft, the Netherlands

Bart Schilperoort
Faculty of Civil Engineering and Geosciences, Department of Water Resources, Delft University of Technology, Delft, the Netherlands

Peter Baas
Faculty of Civil Engineering and Geosciences, Department of Geoscience and Remote Sensing, Delft University of Technology, Delft, the Netherlands, and, Whiffle B.V., Delft, the Netherlands

Marie-claire ten Veldhuis
Faculty of Civil Engineering and Geosciences, Department of Water Resources, Delft University of Technology, Delft, the Netherlands

Bas J.H. van de Wiel
Faculty of Civil Engineering and Geosciences, Department of Geoscience and Remote Sensing, Delft University of Technology, Delft, the Netherlands,
B.J.H.vandeWiel@tudelft.nl

May 17, 2019

Abstract

Wind machines are used to prevent or mitigate the adverse effects of night frost in spring. These frost events occur during clear-sky, low-wind nights in which a thermal inversion builds up from the surface. The machines work by mixing and transporting warm air from aloft downward which consequently erodes the thermal inversion. Various studies have been conducted regarding this frost protection method, which have resulted in empirical regression models that relate affected area and temperature enhancement (i.e. the performance) with inversion strength. In this study, we assessed height-dependent temperature responses and the sensitivity of wind machine performance to various physical processes. Both of which have not been studied thoroughly in earlier works. In this regard, a large field experiment was conducted and experimental analysis was augmented with sensitivity studies using turbulent resolving Large Eddy Simulations (LES).

Experimental observations showed that the temperature response strongly depends on the radial distance to the fan and the height above the surface. In agreement with previous studies, the wind machine was able to achieve rotation-averaged temperature increases of up to 50% of the inversion strength ($\approx$3 K) in an area of 3-5 ha at 1 m height. Furthermore, it was observed that low-speed ambient winds ($<$1 m/s) can cause strong upwind-downwind asymmetries in the protected area, the downwind area being larger.

The LES model, inspired by the field experiment, showed similar spatial temperature responses as compared to observations. Sensitivity studies using a simplified case showed that the affected area strongly increased for slower axial rotation times (ranging from 3 to 6 min) while the temperature enhancement stayed relatively constant. Furthermore, variation of the horizontal tilt angle showed that, in our model, temperature enhancement was maximized between 8° and 16°. Presumably, those angles, corresponding to near horizontal flow, are very effective in generating strong shear layers which in turn generate Kelvin-Helmholtz like instabilities. These processes increase mixing and vertical transport of heat. Finally, analysis on the ambient wind showed that, in agreement with observations, strong upwind-downwind asymmetries in the affected area exist.

1 Introduction

In agricultural applications often wind machines are used to prevent or mitigate the adverse effects of night frost in spring (particularly in the fruit sector) Scharringa (1962); Snyder and de Melo-Abreu (2005). Here we aim to quantify the impact of wind machine operation on the local temperature field in an orchard. To this end, a large field experiment is conducted and experimental analysis is combined with numerical simulation studies in order to assess the functional relations between wind machine performance and the dominating physical processes occurring during radiative frost events. These events typically occur during clear-sky, low-wind (<2.5 m/s) nights in which, due to suppressed turbulent mixing and radiative cooling, a thermal inversion builds up from the surface (Kalma et al. (1992); van de Wiel et al. (2017)). In spring, when crops are blooming and their buts are vulnerable (Snyder and de Melo-Abreu (2005)), these events cause freezing damage with major economic losses as a result (White and Haas (1975); Berz (1992)).

Wind machines are used to reduce these losses by eroding the thermal inversion. This works by blowing large amounts of warm air from aloft downward into the cold canopy (Brooks et al. (1954); Bates et al. (1978)). The resulting local temperature enhancements near the surface will vary depending on e.g.: the strength and direction of the ambient wind, the strength of the temperature inversion of the background flow as well as on wind machine characteristics such as engine power and axis rotation time (Beyá-Marshall et al. (2019)). For a typical machine, 10 m in height and 130 kW of power, a temperature increase between 25% to 50% of the inversion strength can be achieved in areas of 3-5 ha (Evans (1999); Snyder and de Melo-Abreu (2005)). Assessment of this performance has typically been based on empirical results, resulting in rater specific regression models that relate: affected area and temperature enhancement with the inversion strength (Ribeiro et al. (2006); Beyá-Marshall et al. (2019)). In those studies, focus was on local temperature response depending on radial distance to the wind machine. In reality, however, it is expected that, the responses will also depend on the *height* at which temperature is diagnosed. Particularly in nights with radiative frost, temperature variation with height is considerable and it is expected that the same holds for the physiological response of the crop (damage).

In this study we will therefore asses both the horizontal and vertical temperature response. Moreover, were full three-dimensional data is necessarily incomplete in field observation data and conditions cannot be controlled, we will augment our analysis with numerical turbulent-resolving Large Eddy Simulations (LES). As such, the objective of the field experiment is to obtain a three-dimensional picture of the temperature field and to create a so-called high-quality dataset to which simulations can be compared. Hereto, the Distributed Temperature Sensing (DTS) technique is used in combination with a point sensor grid. This provided an order of magnitude higher spatial and temporal resolution as compared to previous studies by e.g. Ribeiro et al. (2006); Beyá-Marshall et al. (2019). With DTS steep temperature gradients can be resolved and temperature can be measured over hundreds of meters Zeeman et al. (2014); Smolen and van der Spek (2003). Here we use the DTS observations to quantify the impact of wind machine operation on the scale of a fruit field.

The LES is used for a theoretical study on the impact of such mixing devices on both the flow field and temperature in a stably stratified environment. The simulations are based on the Basilisk numerical solver, which has recently been used successfully in the study of the atmospheric boundary layer (Popinet (2015); van Hooft et al. (2018b)). First, a comparison between the model outcome and the results from the field campaign is made. It will be shown that the simulations are capable of reproducing the observational findings both in a qualitative and quantitative sense (where it is realized that strong simplifications are made). Next, the simulations are used as a tool to investigate wind machine performance response to changing forcing parameters, like: *external* parameters: prevailing wind speed and temperature inversion strength, and *wind machine design* parameters such as: axial rotation time, horizontal tilt angle and engine power. To asses the sensitivity to these parameters, quantitative performance indicators will be put forward. This allows for the functional relations between these parameters and performance to be investigated.

The study is naturally divided in two parts, the observational and numerical study. An overview of the field experiment is presented in Section 2. The experimental results are analysed and discussed in Section 3. The numerical study is laid out in Section 4 and a similar result analysis follows in Section 5. The main results will be concluded in Section 6.

2 Experimental setup

2.1 Experimental site

The experimental part of our research was conducted between January 15 and February 4, 2019, in a pear orchard in Krabbendijke (Zeeland, the Netherlands, 51°25′44.7″N, 4°8′8.5″E). The trees are 3 m in height, were planted in rows 3 m apart which are oriented 10° West of North. The slope of the field does not exceed 1%. As the experiment was executed in winter, no leaves were present on the trees. In Figure 1, an aerial image of the site is shown. It can be seen that the orchard is separated by a dike from the Oosterschelde, a large estuarine water body.

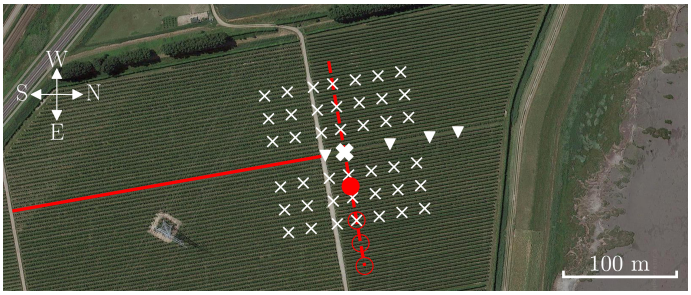

Figure 1: Aerial image of the experimental site. The Oosterschelde is visible on the right side of the image. Markings are explained in the legend of Figure 3. Image adapted from Google Maps.

2.2 Wind machine specifications

The wind machine was installed in 1995 and was manufactured by Orchard-Rite® (Figure 2). It has a 10.5 m hub height and 5 m diameter double-bladed fan which blows 7° downward. The wind machine was powered by a propane engine with a design power of 134 kW and a total runtime of 165 h. The wind machine blades rotated at 540 rpm and the fan top revolved around the tower once every 5 min.

Figure 2: The wind machine in the pear orchard, with the engine mounted at the bottom of the tower. In the back, the dike is visible.

2.3 Measurement setup

The objective of our setup was to obtain a three-dimensional impression of the temperature field around the wind machine. Hereto, we combined horizontal grids of point observations (at two vertical levels), with Distributed Temperature Sensing (DTS) providing both detailed vertical profiles and horizontal line observations. Wind measurements were taken during fan operation to asses the wind speed as a function of distance from the wind machine. Additionally, on-site weather stations were installed in order to capture the local meteorology. This setup is shown in Figure 3.

Distributed Temperature Sensing (DTS) is a technique to measure the temperature along a fiber optic cable with high spatial (0.3 m) and temporal resolution. This is done using the temperature dependent backscatter signal of a laser pulse (Smolen and van der Spek (2003); Selker et al. (2006)). Two different cables were used, a thick 6 mm PVC reinforced duplex fiber optic cable (response time of ≈5 min) and a thin 1.6 mm fiber optic cable (≈30 s). Both were measured using a Ultima-S^{TM} system (Sillixa Ltd.). The thick cable was deployed in a double-ended configuration by looping back through the second core. Both, forward and backward measurement were averaged over 5 s. The thin cable was used in a single-ended configuration, with an averaging period of 10 s. For calibration, the cables went twice through a well-mixed water bath which was monitored by a Pt100 temperature probe. The calibration was done using the internal reference of the Ultima, and the bath, in combination with the python DTS calibration package by Tombe and Schilperoort (2019). For the single-ended configuration this setup can result in a bias, however this appeared insignificant for our results. Using this setup ≈0.1 K of temperature accuracy is achieved.

The configuration of the cables is shown in Figure 3. The thick cable of near 300 m length was oriented North-South and placed at ≈1 m above the surface. The thin cable ran 100 m East and 80 m West of the wind machine at a height of ≈1 m and 0 m (along the surface). Additionally, the thin cable was used to measure four vertical temperature profiles. An 8 m profile using a pneumatic tower and three 3 m profiles that were supported by metal structures between the vegetation. The DTS setup was used when a radiation frost event occurred during a so-called *high intensity observational period*. These were defined as nights with a temperature near or below 0 °C, wind speeds of less then 2.5 m/s and cloud cover of less than 20%.

For the horizontal grids, 84 tempmate.® M1 temperature loggers (logging interval 1 min) with an external temperature sensor were used. The sensors have a resolution of 0.1 K, an accuracy of 0.5 K and a response time of 30 s. Using the sensors, a 120 m by 120 m grid was constructed at 1 m and 2 m heights as shown in Figure 3.

Wind measurements were done using two types of handheld devices. Four Peakmeter® MS6252B propeller anemometers (accuracy ±2%, sampling frequency 2.5 Hz) and two Testo, Inc. 405i hot-wire anemometers (±(0.1 m/s + 5%), 0.5 Hz). The six devices were mounted on top of a 3 m height tripod. Because of the superior sampling frequency, the propeller anemometers were used to measure the wind speed induced by the fan, while the hot-wire anemometers were used to measure the background wind.

Four Davis® Vantage Pro2 weather stations were installed to provide additional weather information and logged with an interval of 10 min.

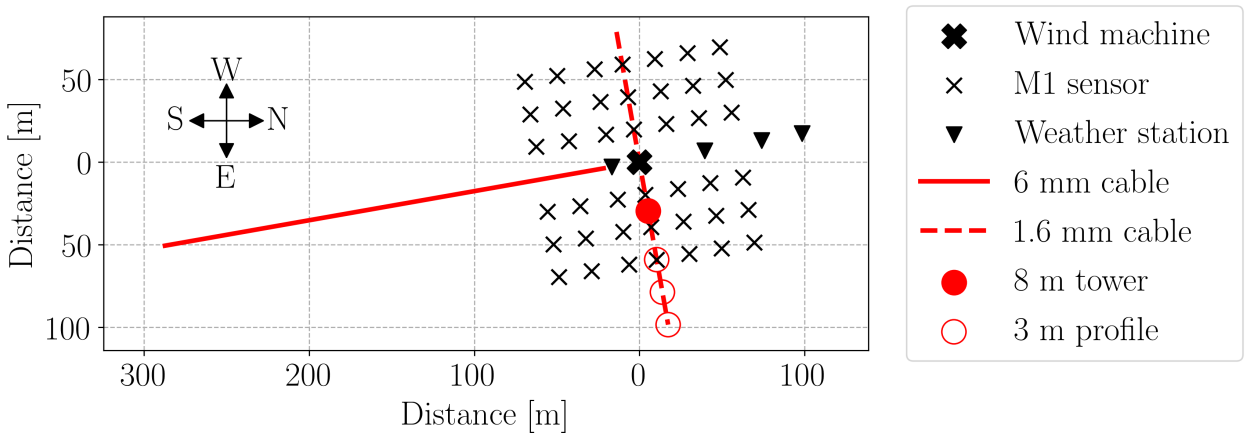

Figure 3: Schematic of the setup with relative distance to the wind machine. The red elements are constructed using DTS.

3 Experimental Results

3.1 Local Weather Conditions

During the experimental period, one radiative frost night occurred on January 20. As a winter case is considered, temperatures were low in general over the full diurnal cycle. The temperature as measured by the weather station of Woensdrecht (10 km East of Krabbendijke), is shown in Figure 4. This station is used, since it was undisturbed by wind machine operation and reported cloud cover. It can be seen that surface temperature responded strongly (≈2 K) to the passing of semi-transparent altocumulus clouds. Apart from this period, the night was predominantly clear sky and the 10 m wind, coming from the East, dropped below 1 m/s (not shown). During the experiment the Oosterschelde had low-tide, which favours the occurrence of stable conditions (see Appendix A.1).

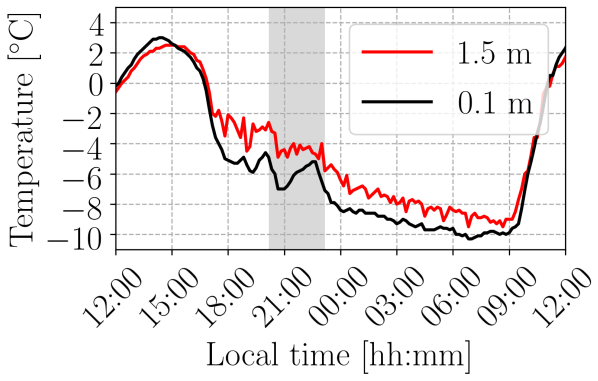

Figure 4: Temperature at Woensdrecht starting noon January 20. The shaded area indicates the passing of semi-transparent altocumulus clouds. Local time was UTC+1.

Where temperature observations at Woensdrecht represent two levels only, a more detailed vertical profile was obtained on-site, as to characterize the nocturnal inversion strength. The average profile around 00:00 at Krabbendijke is shown in Figure 5 (black line). The 'off' and 'on' periods refer to ventilator operation and will be elaborated on later. A typical S-shaped inversion is visible, with the curvature appearing near the surface and the canopy height (3 m). The first being due to the radiative cooling and the second being due to the suppression of turbulent mixing by the canopy. The, $T_{15} - T_{1.5}$, inversion strength, as often reported in literature, was in the order of 3 K. This classifies it as a moderate to strong inversion (Evans (1999)).

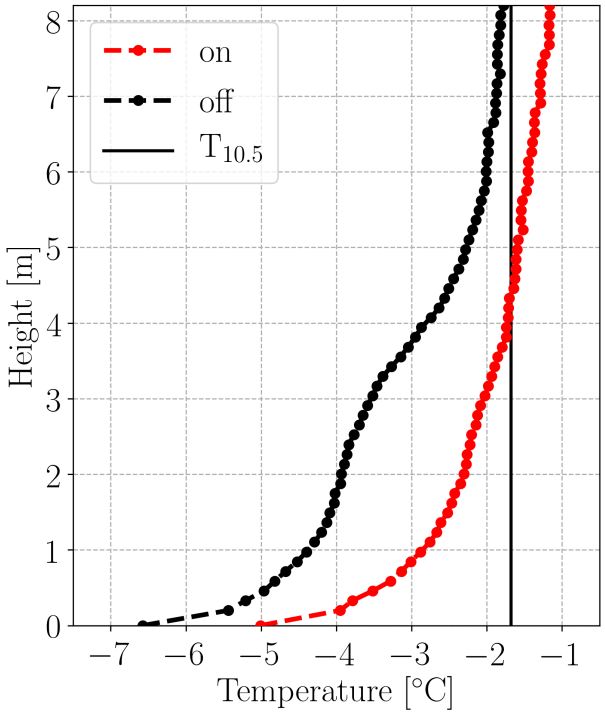

Figure 5: Averaged vertical temperature profiles using DTS for the fan on and off periods. The 10.5 m temperature is based on a linear extrapolation of the 'off' profile top 2 m.

In the figure, hub height temperature (at 10.5 m) is estimated from the linear extrapolated 'off' profile and plotted as vertical black line. In case of 'optimal' mixing, the temperature at the surface would tend towards this temperature. Hence, the maximum temperature increase is defined as

$$\Delta T_{max}(h) = T_{10.5} - T(h) \quad (1)$$

in which $T(h)$ is the undisturbed, 'fan off', temperature at a certain height, h. This will be used later on to normalize results to allow for a comparison between heights.

3.2 Wind machine operation and generated airflow characterisation

Wind machine operation started at 21:48 and stopped at 23:42 (UTC+1), using 100 L of propane gas. From before the start of operation till 23:06, semi-transparent altocumulus clouds were present on-site. The analysis will focus on the clear sky period from 23:06 onwards, assuming minimal effect of the preceding cloud period.

When in operation, the wind machine accelerates a a finite 'cone-form' volume of air. This volume is refereed to as the *jet*. When seen from above and in the absence of wind, the jet sweeps a circular area due to the hub rotating on the fan tower. The maximum local speed of the passing jet was measured at 3 m height as a function of distance to the fan (Figure 6). The measurement period spanned one hour during which the 3 m mean wind (0.5 ± 0.3 m/s) came from the East-Northeast ($67 \pm 4°$). A strong, ≈2 m/s, upwind-downwind (East-West) asymmetry is visible. Interestingly, due to the fan elevation at 10 m (blowing down at 7°), the closest observation at the East side appears to be below the jet.

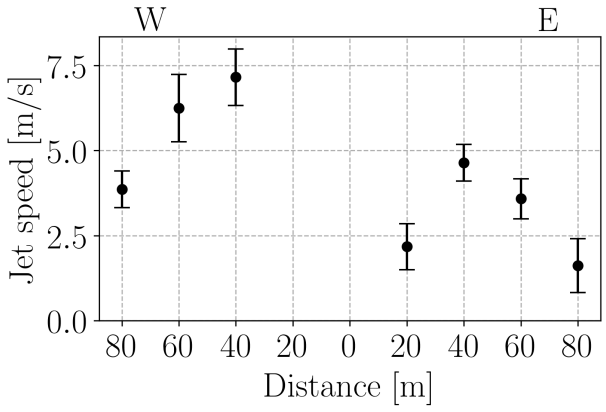

Figure 6: Jet speed based on four handheld vane anemometer measurements at a height of 3 m. W-E refers to the West and East-side of the ventilator (with main wind from the East).

3.3 Horizontal temperature response and influence distance

The temperature measurements done using the horizontal DTS cables are shown in Figure 7 in which time is expressed relative to the starting time of the wind machine. As in the Woensdrecht data, when the clouds disappeared a clear drop in temperature was measured. In addition, the 5 min rotation period of the wind machine can be identified. Note that the data in Figure 7a is 'smeared' out as compared to the others due to the slower response time of the cable (5 min vs 30 s). The light 'yellow bar' in Figure 7b and 7c represents a strong temperature signal due to heat released by the engine reaching 15 °C and 40 °C, respectively. Although the majority of this heat may 'leave' the system through vertical convection, it does have the potential to raise the temperature in addition to the ventilator. The average energy consumed by the engine was ≈370 kW, generating ≈240 kW in heat. This is equivalent to an air volume of $\approx 10^5$ m^3 being raised by 1 K over one rotational period, 300 s.

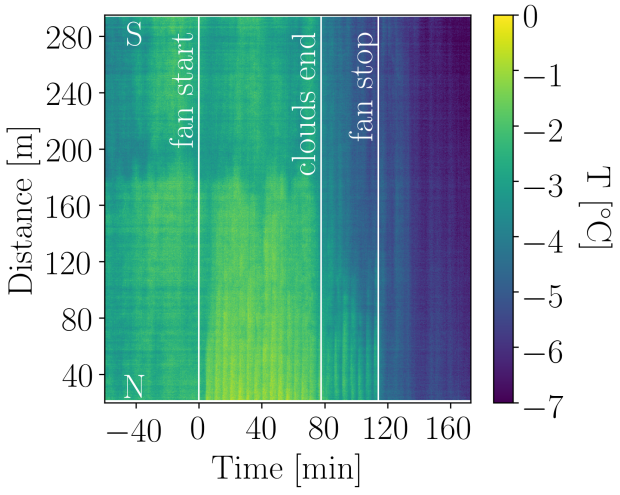

(a) South cable at 1 m height.

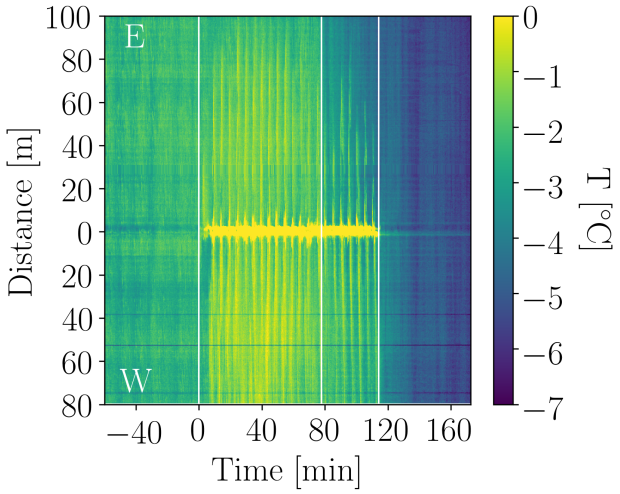

(b) West-East cable at 1 m height.

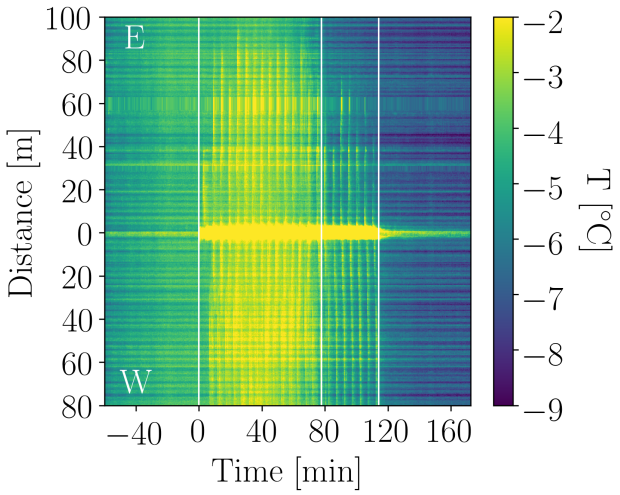

(c) West-East cable at 0 m height.

Figure 7: Time series of the horizontal DTS measurements. Events are indicated by the white lines. Clouds were present before the start of this time series. NWSE denote the orientation of the cables.

In case of a steady state condition, the average temperature change caused by the wind machine could be assessed by simply subtracting the temperature before fan operation ('reference state', fan off) from the temperature after a few rotations (fan on). However, the clear sky conditions

of interest only appeared during fan operation. Therefore, our reference state is defined after operation, averaged from 119 min to 134 min. The fan on period is chosen accordingly and averaged from 88 min to 108 min, spanning 4 rotations. The results are shown in Figure 8.

For the South cable, Figure 8a, a spatial North-South slope in the temperature is visible during the fan off period. We hypothesize that this is due to a 'thermal memory' in the system. Figure 8b is perpendicular to 8a and aligns with the mean wind direction. As with the jet speed (Figure 6), an upwind-downwind asymmetry is present. Note that the sharp temperature 'spikes' in Figure 8c are no artifacts but are caused by differences in soil cover. The signal had a spatial periodicity of 3 m, which coincides with the row spacing. As shown in Appendix A.2, the surface directly under the trees was covered with litter and composting leaves, whereas in between the tree rows matured grass was present.

To determine to the average temperature change from Figure 8, the black line cannot simply be subtracted from the red line, due to the overall temperature trend that occurred during the night (compare also Figure 4). This can be corrected for by using a height dependent reference temperature which was not influenced by the wind machine. This reference was chosen based on wind direction and the temporal responses seen in Figure 7. For the 1 m height measurements, the averaged South section temperature from 270 m to 280 m was taken as a reference (Figure 8a). For the 0 m height measurements, the averaged East section temperature from 91 m to 100 m was taken (Figure 8c).

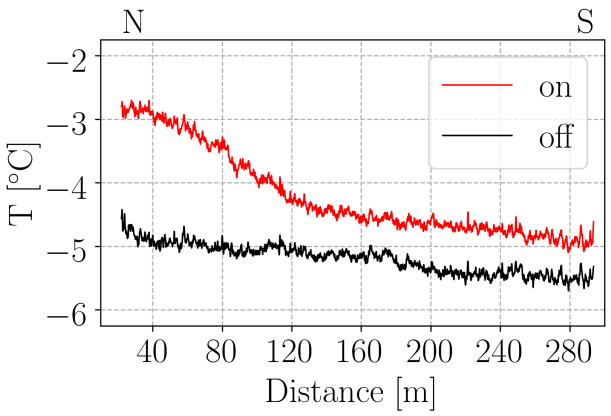

(a) 1 m height South cable.

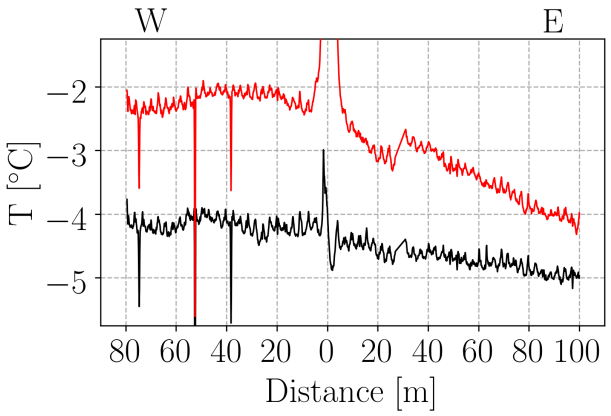

(b) 1 m height West-East cable.

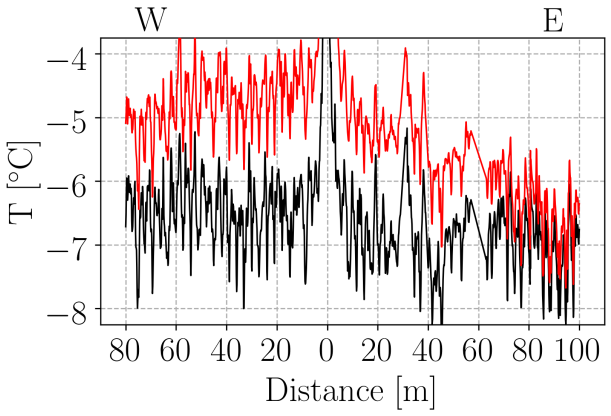

(c) 0 m height West-East cable.

Figure 8: Horizontal DTS measurements averaged over the fan on and fan off periods. NWSE denote the orientation.

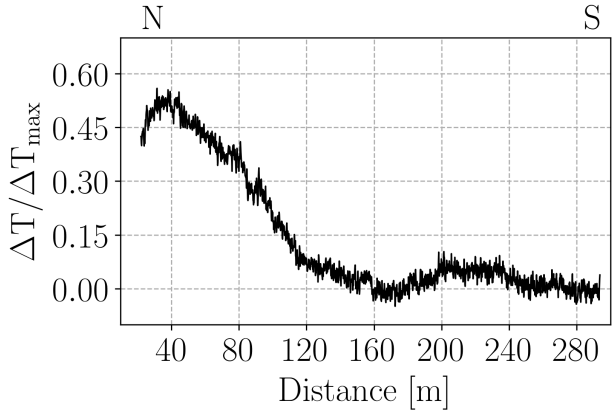

(a) 1 m height South cable, $\Delta T_{max} = 2.75$ K.

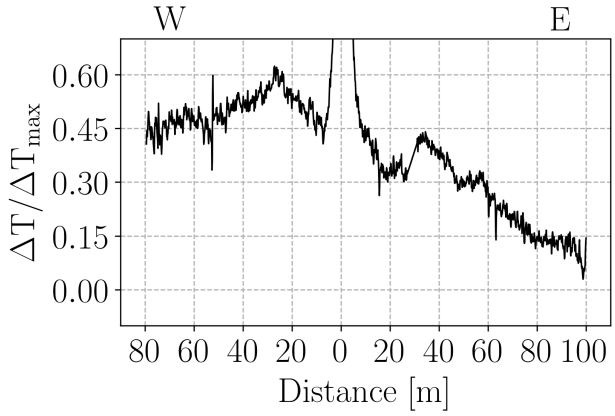

(b) 1 m height West-East cable, $\Delta T_{max} = 2.75$ K.

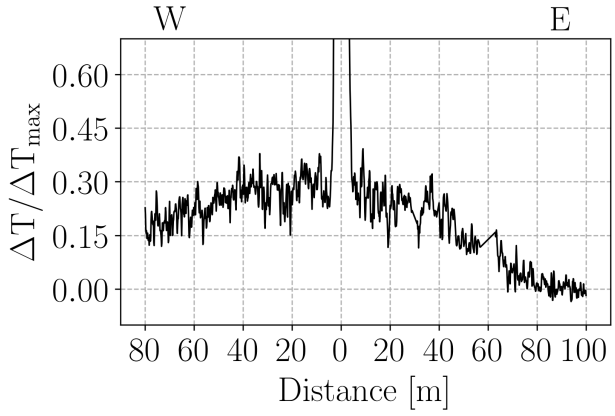

(c) 0 m height West-East cable, $\Delta T_{max} = 4.99$ K.

Figure 9: Efficiencies for the horizontal DTS sections. NWSE denote the orientation.

Using the South cable from Figure 8a as an example: The 270 m to 280 m temperature is averaged, after which both the red and black curve are offset by this reference temperature. They are then subtracted from each other to get the temperature change due to fan operation at every location along the cable. This temperature difference can formally be expressed as,

$$\begin{aligned}\Delta \mathrm{T}\left(\vec{r}\right) = &\sum_{t\in \mathrm{on}} \left(\mathrm{T}\left(\vec{r},t\right) - \mathrm{T}_{\mathrm{ref}}\left(h,t\right)\right) \\ &- \sum_{t\in \mathrm{off}} \left(\mathrm{T}\left(\vec{r},t\right) - \mathrm{T}_{\mathrm{ref}}\left(h,t\right)\right)\end{aligned} \tag{2}$$

in which h is the height of the location vector $\vec{r}$, time t is in the fan 'on' or 'off' period, T is the measured temperature and $\mathrm{T}_{\mathrm{ref}}$ is the reference temperature as explained before. This procedure is carried out for all three horizontal DTS sections. Afterwards, these temperature changes are normalized by $\Delta \mathrm{T}_{\mathrm{max}}\left(h\right)$ as defined in equation 1 and the results are shown in Figure 9. The ratio of ΔT over $\Delta \mathrm{T}_{\mathrm{max}}$ will be referred to as the *efficiency*.

To asses the distance at which the wind machine had an effect, the *distance of influence*, a criterion needs to be defined. In literature often the distance at which a certain temperature fraction of the inversion strength is reached is used (Ribeiro et al. (2006); Beyá-Marshall et al. (2019)). Here however, a Gaussian model is introduced which fitted well to the efficiency data in Figure 9. This method works as follows; a priory a Gaussian curve, equation 3, is assumed for the temperature influence as a function of distance at a certain height.

$$f\left(r\right) = \mathrm{a}\exp\left(-\frac{\left(r-\mathrm{b}\right)^2}{2\mathrm{c}^2}\right) + \mathrm{d} \tag{3}$$

This function is least square error fitted to the efficiency curves by varying a, b, c, and d. This is illustrated by Figure 10. We define the distance of influence as b + c and the fitted maximum efficiency as a + d.

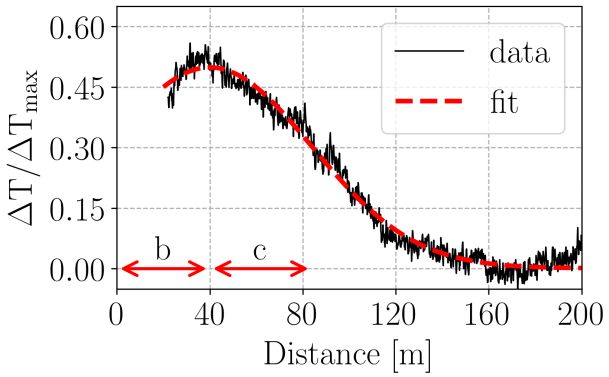

Figure 10: Illustration of the Gaussian model. Fit to Figure 9a. Arrows indicate the fitted values for the parameters b and c. The red curve has per definition a height of a + d.

This model is applied to all the horizontal DTS measurements resulting in the fitting parameters shown in Table 1.

In general, the Gaussian model fitted well and captured the observed asymmetries between East and West. Note that the fitting error became large when the efficiency did not yet approach zero. Based on these influence distances and Figure 9 the area in which a temperature enhancement was achieved is crudely approximated to be 3-5 ha at 1 m height.

Table 1: Distance of influence and maximum efficiency based on the Gaussian fit. Least square error fit uncertainties are reported when greater than the least significant digit.

Section	Distance [m]	Max Efficiency
South 1 m	83.9 ± 0.3	0.50
West 1 m	104.7 ± 76.3	0.53
East 1 m	67.8 ± 1.3	0.37
West 0 m	76.6 ± 29.5	0.53 ± 0.01
East 0 m	51.5 ± 0.6	0.44 ± 0.01

3.4 Mixing efficiency profiles and temporal responses

The 8 m averaged vertical profile was shown in Figure 5. To get the efficiency for all four vertical temperature profiles, the same procedure as in the previous section is used. The background temperature was corrected for by using the 1 m height reference (average over South section from 270 m to 280 m), which was taken to be representative for the whole canopy. These results are shown in Figure 11.

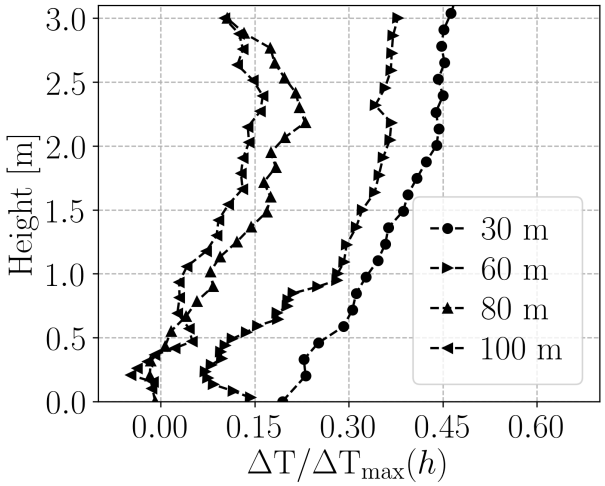

Figure 11: Reach into the canopy on the East side of the wind machine. The distances relative to the fan are shown in the legend. Note that $\Delta \mathrm{T}_{\mathrm{max}}$ is height dependent.

There is an interesting dependence on distance: the further away from the fan the more the temperature enhancement is confined to the canopy top. Close to the fan, the flow over the canopy is strongest as is the difference of flow magnitude with the (slow) in canopy flow. Presumably, vertical mixing is generated by Kelvin-Helmholtz instabilities as often encountered in flows over canopies (Boing et al. (2010); Finnigan et al. (2009)). As those effects are strongest near the fan, there mixing will penetrate more effectively. Note that the cold biomass and strong inversion near the surface could play a role in damping this penetration. To study this behaviour further, temporal responses at different heights are shown in Figure 12.

The 5 min fan revolution cycle causes ≈3 K of temperature variation at 0 m and 0.2 m height, damping to ≈2 K at 2 m and less than 1 K at 8 m. This amplitude difference is in part explained by $\Delta \mathrm{T}_{\mathrm{max}}$ decreasing with increasing height. Note that after each temperature ramp, cooling of the air towards its reference state is faster near the surface which could be a result of the cold biomass present. Interestingly, the 0 m measurement laying on grass and 0.2 m measure-

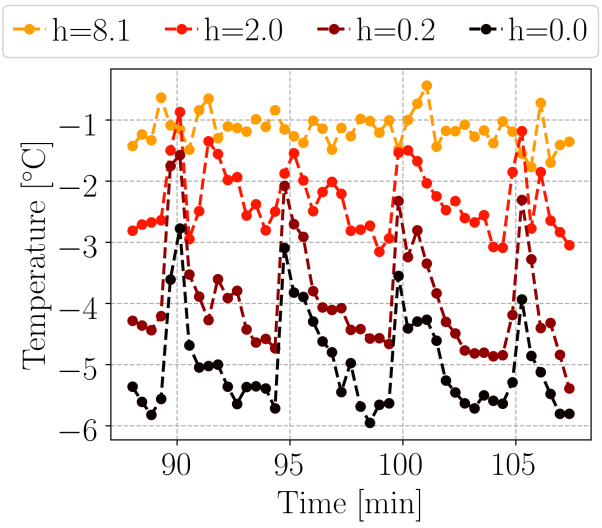

Figure 12: Temperature response at different tower heights, 30 m East from the wind machine.

ment just above, had a similar amplitude and decay. Hence at this location, no extra 'damping' of the temperature signal due to direct contact with the grass was measured.

3.5 Efficiency contours

Using the sensor grid, the goal was to get two-dimensional plane measurements at two heights. Due to water/frost damage, the grid data at 2 m height was lost. For the 1 m data the same procedure was used as before to get the efficiency. The contour plot is shown in Figure 13.

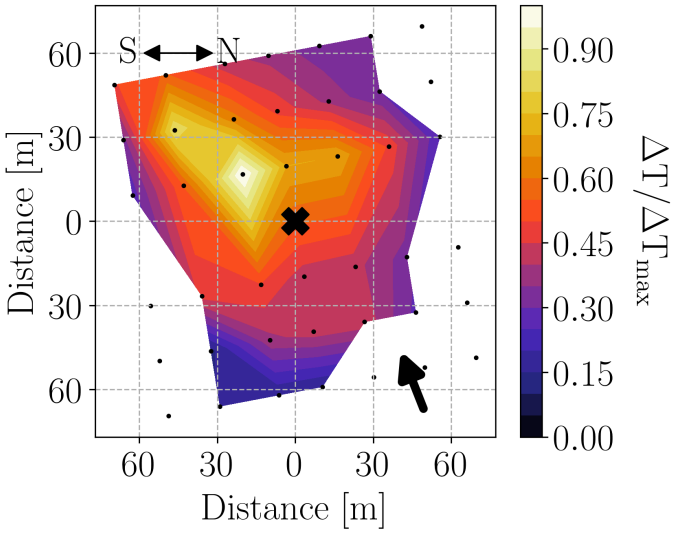

Figure 13: Efficiency contours near the wind machine at 1 m height using the M1 loggers (dots). At missing data points water/frost damage occurred. The wind direction is denoted by the arrow.

The wind direction is distinctly recognizable. Also, the affected area is larger than the size of the grid network, which agrees with the previous analysis of the DTS showing that this area is 3-5 ha. Finally, note that the impact of engine heat may be visible as well, as the efficiency exceeds 1 near the fan.

4 Simulation Methods

In order to further study the dynamics of wind machine operating in a stable stratification, simulations with Large-Eddy Simulation (LES) model are performed. This approach facilitates to study the local dynamical response to changing forcing parameters. We focus on the effects of *external* parameters such as: the prevailing wind speed (U) and the strength of the temperature inversion (N), and the parameters that govern the the *wind machine design*: the rotation time (τ), the engine's power output (P) and rotor tilt angle (α). (see Figure 14).

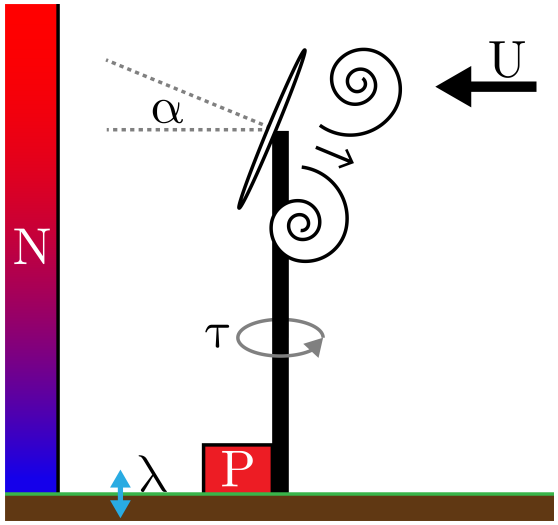

Figure 14: Schematic of the simplified model involving the wind machine. *External* parameters: the prevailing wind speed (U) and the strength of the temperature inversion (N). *Wind machine design* parameters: the rotation time (τ), the engine's power output (P) and rotor tilt angle (α). λ denotes the surface coupling of equation 4.

4.1 The numerical solver and modelled physics

The LES is based on the partial differential equation solver Basilisk which is available at `www.basilisk.fr` (Popinet (2015)). For details on the model we refer to van Hooft et al. (2018b). The numerical model solves the filtered Navier-Stokes equations under the Boussinesq approximation (Wyngaard (2010)). The solver is second order accurate in space and time and uses a fractional-step method (Castillo-Castellanos (2017); Popinet (2009)). The advection term is computed using the Bell-Collela-Glaz scheme and the pressure is calculated using a multi-grid strategy (Bell et al. (1989); Brandt (1977)). The turbulent mixing of heat and momentum at the sub-grid scale is parametrized with the eddy-viscosity closure formulated by Vreman (2004).

Due to the strongly localized dynamics around the wind machine, an adaptive octree based grid is used (see van Hooft et al. (2018b)). In this work, grid adaptation is based on an estimated discretization error in the solution fields for the wind components and temperature. The error thresholds or so-called 'refinement criteria', are set to 0.5 m/s and 0.3 K, respectively, balancing numerical accuracy and computational effort (see van Hooft et al. (2018a)).

Besides the Navier-Stokes equations and eddy-viscosity closure, the modelled physics consist of: a soil scheme,

a wind forcing, a wind machine momentum source and a source representing engine heat. The soil scheme is based on simple land-atmosphere coupling similar to van de Wiel et al. (2017) and is implemented as in van Hooft et al. (2019). In these works the soil heat flux F [$\mathrm{Jm^{-2}s^{-1}}$] is determined according to

$$F = \lambda \left(\mathrm{T_{surf}} - \mathrm{T_{soil}} \right) \tag{4}$$

in which λ [$\mathrm{Jm^{-2}s^{-1}K^{-1}}$] is the soil-heat coupling strength, $\mathrm{T_{surf}}$ the surface temperature, and $\mathrm{T_{soil}}$ a fixed soil temperature. The wind forcing is implemented near the horizontal boundaries (10% of the domain size) as a slow relaxation towards a profile. In this volume the temperature is also forced, to simulate the advection of 'fresh' air. The wind machine momentum source is based on a power formulation (Appendix B.1) in which power can be interpreted as the work done on the air per unit time. It is assumed that the process generating this power has an efficiency of 10%, such that the remaining 90% is released as heat.

Note this model is a crude simplification of complex reality and therefore is necessarily incomplete. Specially, here we have omitted, amongst other things, to implement the geometry of tree rows, have assumed horizontal homogeneity, no background turbulence is present (VSBL), and no surface drag closure is implemented. Here we aim for simplicity to study qualitative behavior due to ventilator operation. Things such as the realistic implementation of tree geometry is beyond the scope of the present study (e.g. Finnigan et al. (2009)).

4.2 Simulation setup

Two cases are defined. The setup of the first case is inspired by the experimental setting in order to enable a comparison between model results and observations. The second case uses idealized settings and is used for sensitivity studies.

In both a 700^3 $\mathrm{m^3}$ domain is chosen with periodic boundary conditions in the horizontal dimensions. The bottom and top boundary conditions are set to no-slip and stress-free, respectively. The maximum resolution is set to 512^3 corresponding to a minimum grid size of ≈1.37 m. The wind machine momentum forcing is turned on after 30 s and the simulation runs for four fan rotation periods.

For the Krabbendijke case, the wind machine hub height is set to 10.5 m, rotor diameter to 5 m, $\tau = 300$ s and $\alpha = 7°$. The power of the wind machine, P, is set to ≈14 kW based on a jet velocity comparison between simulation and observation. The initial wind profile, U, is prescribed to be logarithmic, according to equation 5, and can be changed in magnitude using the prefactor U_f. Here, $\mathrm{U}_f = 0.1$ such that the wind speed at the hub height is ≈0.5 m/s.

$$\mathrm{U}(h) = \max\left(\mathrm{U}_f \ln\left(\frac{h}{0.1} \right), 0 \right) \tag{5}$$

The initial temperature profile is assumed to be logarithmic with height, equation 6, such that it fitted the observed profile. However, the S-shape is omitted and the profile shifted such that $\mathrm{T_{surf}}$ is 0 °C. $\mathrm{T_{soil}}$ is set accordingly to 0 °C.

$$\mathrm{T}(h) = \max\left(\ln\left(\frac{h}{0.2} \right), 0 \right) \tag{6}$$

After initialization, the temperature and wind profiles are forced at the boundaries as described in the previous section. The soil-heat coupling strength, λ, is chosen as 5 $\mathrm{Jm^{-2}s^{-1}K^{-1}}$ which represents the coupling of a grass surface van de Wiel et al. (2017).

For the sensitivity study a new standard case is defined from which individual parameters are varied. The same domain, resolution, boundary conditions, surface coupling, soil temperature and wind machine settings are set as in the Krabbendijke case. However, from the wind machine parameters, the rotation period is shortened to 240 s and the engine heat is turned off. Default, the wind profile is set to zero and when wind speed is analysed, U_f is varied (equation 5). For temperature, a simple linear profile with a slope of $\mathrm{N^2} = 0.3$ K/m is set:

$$\mathrm{T}(h) = N^2 h \tag{7}$$

During simulations, diagnostics are performed similar to the DTS and wind measurements done during the field experiment. These have a 1 m spatial and 1 s temporal resolution. In the analysis numerical results are taken at the same location as the observations as to allow comparison. In addition, four temperature slices at 0.5, 1, 2, and 4 meter height are outputted with a 2 m spatial and 5 s temporal resolution.

The descriptive overview of the setup herein can not do justice to all the exact details of the implementations. As such, the used methods are documented and are made freely available via the Basilisk website: `www.basilisk.fr/sandbox/vheusinkveld`, Krabbendijke case: `/krabbendijke.h`, idealized case: `/idealized.h`.

5 Simulation Results

5.1 Comparison with observation

The maximum speed of the passing jet was averaged over the four rotations and is shown in Figure 15. The 2 m/s asymmetry in maximum jet speed between West and East as seen in the experimental data was not present. However, a similar upwind-downwind asymmetry is seen in the decay of the jet speed with distance.

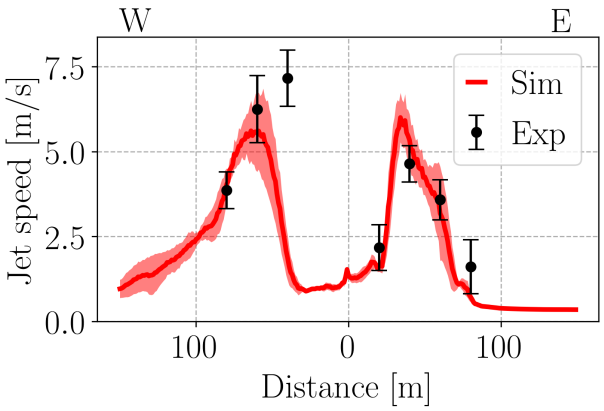

Figure 15: Jet speed comparison between the simulation and experiment. The shaded area represents the standard deviation over four rotational averages of the maximum jet speed.

For comparing the DTS temperature measurements, the experimental 'clear sky, fan on' data was used. This data was shifted in time such that a passing of the jet occurred synchronous with the simulation data. The results are shown Figure 16 for which the experimental data was offset by 5.5 K. In general, there is a remarkable qualitative agreement between simulation and experiment considering the limited physics that was implemented. This suggests that the most dominant processes were taken into account. Besides this, the simulation data shows more detail due to the instantaneous response time and higher sampling as compared to the field experiment.

The vertical time series, Figure 16a, shows the temperature responses near the surface lasting longer in the simulations with transitions being sharper. Horizontally from West to East, Figure 16b, upwind (East) temperature responses were similar between experiment and simulation at equal distances while downwind (West) responses showed a discrepancy. The latter might be a consequence of the observed differences in jet speed (Figure 15). The horizontal North-South time series, Figure 16c, also shows similar temperature responses at equal distances. Note that the response to the first rotation is distinctly different from the others. This is caused by the simulation start-up, with temperature and wind fields being disturbed for the first time. For this reason, the analysis will focus on the three rotations thereafter.

From the numerical data, a horizontal slice at 1 m is taken to determine the efficiency in this plane. The procedure differs slightly as compared to the experiment since the temperature field is initialized and thus known. In general the procedure is as follows:

1. The temperature field is averaged over the last three rotations and the initialized temperature field is subtracted. Thus getting the average temperature change.

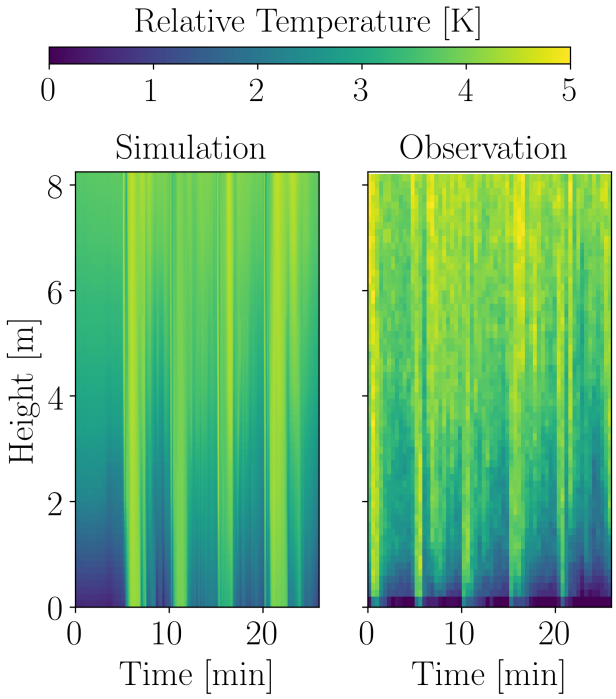

(a) Vertical cable, 30 m East of the fan.

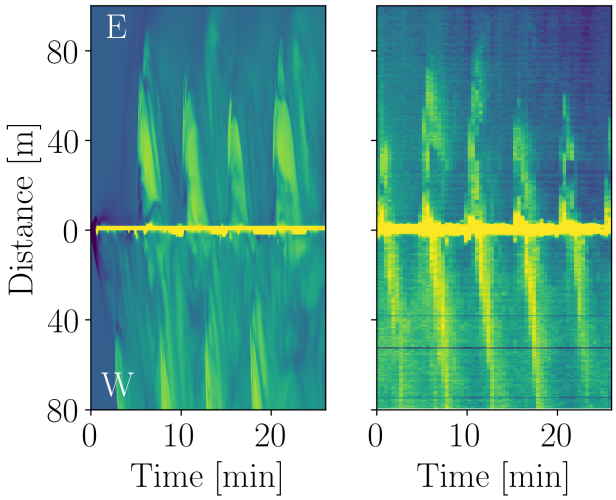

(b) Horizontal West-East cable. Note: ambient wind is from the East.

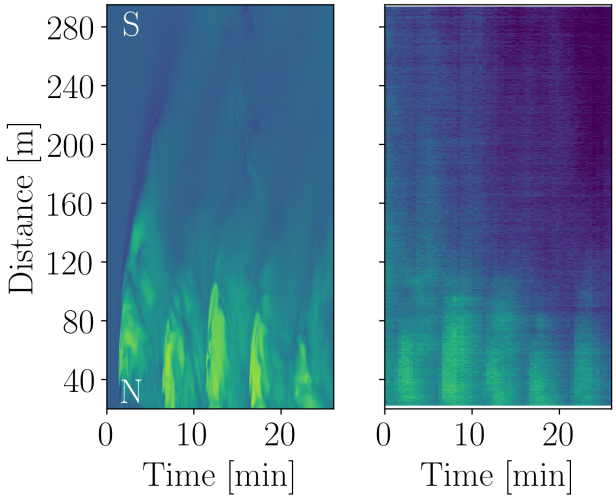

(c) Horizontal North-South cable.

Figure 16: Time series comparison between the DTS measurements of the simulation (left) and the experiment (right).

2. A slice is chosen at a particular height, h, and is normalized by ΔT_{max} (equation 1, using the temperature profile as defined in the simulation), to get the two-dimensional efficiency.

For the slice at 1 m height the result is shown in Figure 17. Simulated efficiencies reached similar values as in the experiment and the wind direction is distinctly visible. However, based on the comparisons made in Figure 15 and 16b this wind dependence may be slightly overestimated.

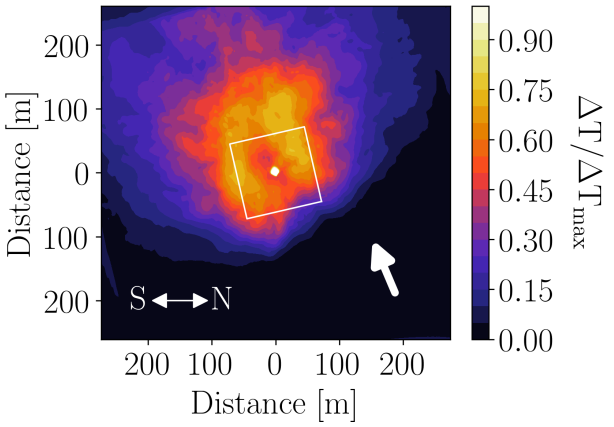

Figure 17: Efficiency at 1 m height with $\Delta T_{max} = 1.96$ K. The arrow denotes the wind direction and the white square the area spanned by the sensor grid in the original field experiment, Figure 13. Note that the white central circle is a results of the engine heat surpassing efficiencies of 1.

5.2 Sensitivity to forcing parameters

The comparison in the previous section shows that the model is able to mimic the response of the temperature field due to fan operation. In this section, we aim to quantitatively compare changes as a result of varying parameters. For this, a performance measure needs to be defined. The full three-dimensional temperature field could be investigated. However, this data is high in dimensionality and does not directly reflect things that are of practical importance, namely:

- What is the area influenced by the wind machine at different heights?
- What is the achieved average temperature increase or efficiency in this area?

These will be denoted as the *performance measures* and will be defined as follows:

1. A two-dimensional efficiency slice is made as described in the previous section. An example of this is shown in Figure 18.
2. For every (discretized) angle in the plane, the distance of influence is estimated using a Gaussian fit (similar to the example in Figure 10) denoted by the white dashed line in Figure 18.
3. The area enclosed by this line is defined as the influenced area. The efficiency in this area is averaged to get the other measure.

Thus the 'performance' of the wind machine can, per simulation run, be summarized to: the influenced area and the area averaged achieved efficiency.

Notice that for runs without a mean wind, the problem is axisymmetric in the horizontal, centred around the wind machine. Consequently, the measure of area can be reduced to a measure of distance (area $= \pi\,(\text{distance})^2$). The standard deviation of this distance (measured per angle) is used as an estimate for the variability in results between repeated simulations. For Figure 18 this resulted in an influence distance of 81 ± 5 m and an average efficiency 0.46 ± 0.02.

In the next subsections, the analysis will be focussed towards functional relations between parameters and the performance measures. Hereto, only the results for the 2 m height are shown. For completeness, also a true ensemble simulation of 5 times a rerun of the reference case is included in the results.

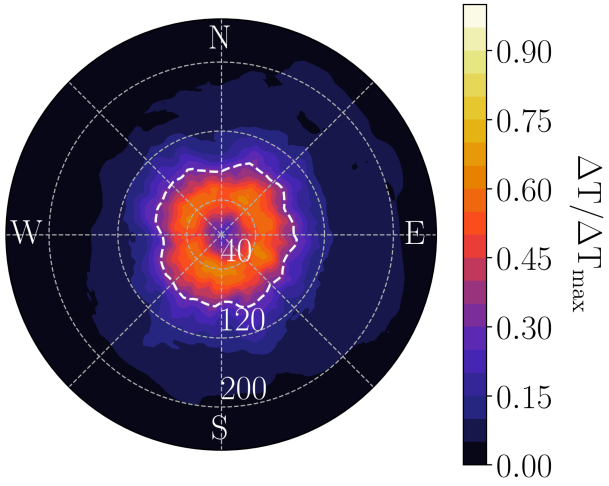

Figure 18: Example showing efficiency in a two dimensional contour plot. The radial distance is in meters. The white dotted line denotes the distance of influence as fitted using the Gaussian model.

5.2.1 Rotation time: area vs efficiency

The rotation time, τ, was varied between 120 s and 360 s. The total simulation runtime was kept equal to have a constant displaced air volume between runs. The performance measures are shown in Figure 19. For the longer rotation times ($\tau > 240$ s) averaging was done over two rotation cycles only. The influence distance increased linearly with τ, hence area $\sim \tau^2$. This is surprising considering that, time averaged, every location had the same 'jet exposure'. Furthermore, as influence distance increased, efficiency decreased, making apparent that there exists a trade-off between temperature increase, and protected area.

5.2.2 Tilt angle: an optimum?

The tilt angle, α, was varied between 0° and 20°. The resulting influence distance and efficiency are shown in Figure 20. The influence distance decreased with increasing angle, which is expected based on the geometry of the problem. Interestingly enough, in the efficiency an 'optimum' was present between 8° and 16°. In steep visualisations of the flow (not shown) it is observed that for the larger angles less mixing occurred and that the warm jet deflected upward as a result of an increased buoyancy. Hence, the optimal angle corresponds to near horizontal flow. Presumably, this optimized vertical heat transport is caused

by shear driven instabilities (Kelvin-Helmholtz like), which typically are generated at jet flow interfaces.

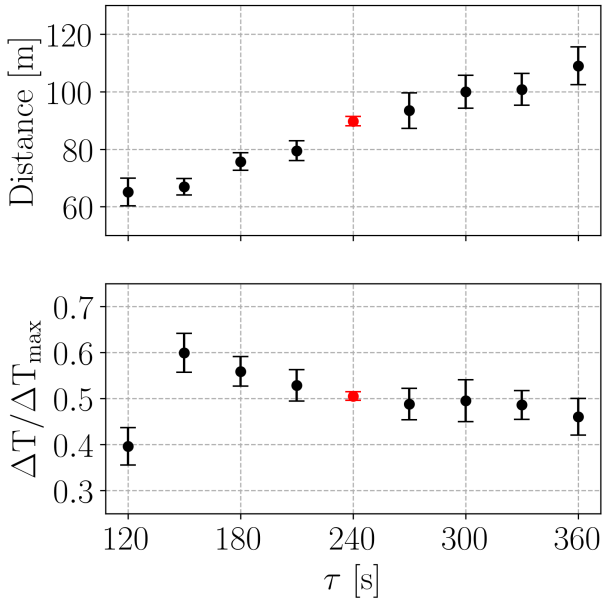

Figure 19: Influence distance and efficiency as a function of rotation time. The error bar is an estimate for the variation between runs. Red denotes the five-member ensemble runs.

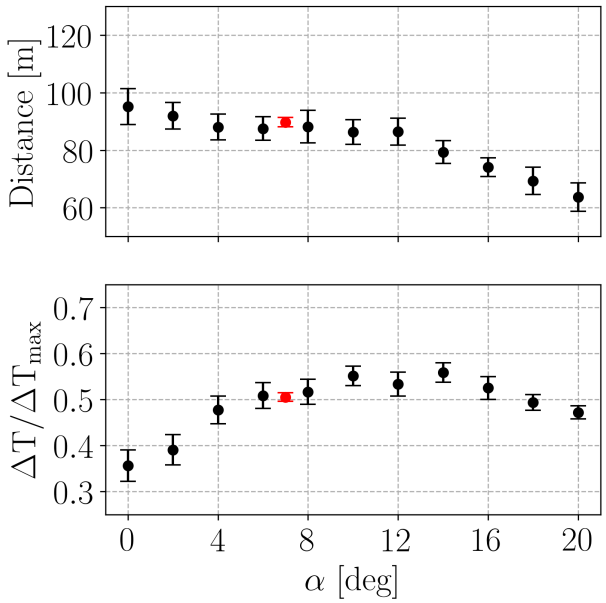

Figure 20: Influence distance and efficiency as a function of tilt angle. The error bar is an estimate for variation between runs. Red denotes the five-member ensemble runs.

5.2.3 Engine power: linear with heat content

The engine power, P, was varied. However, for reasons of clarity, the estimated maximum speed due to the wind machine forcing is reported, denoted as the center jet speed ($\sim P^{1/3}$, see Appendix B.1). The resulting influence distances and efficiencies are shown in Figure 21. The influence distance got larger with increasing jet speed, which is expected due to the higher kinetic energy of the air. Likewise, as distance increased, so did the efficiency. This may be explained by the increased volumetric flow rate, transporting more warm air downward. When translated to power and area, the linear relations become: area $\sim P^{2/3}$ and efficiency $\sim P^{1/3}$. The product implies that the heat content in given slab increases more or less linearly with power.

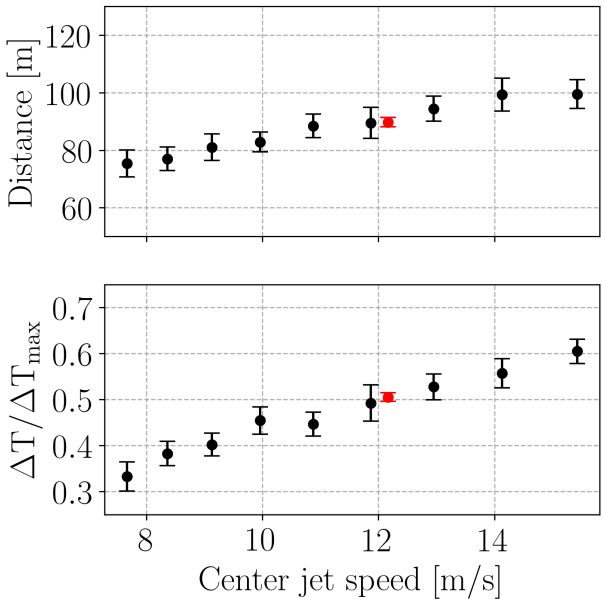

Figure 21: Influence distance and efficiency as a function of center jet speed ($\sim P^{1/3}$). The error bar is an estimate for the variation between runs. Red denotes the five-member ensemble runs.

5.2.4 Ambient wind: a strong asymmetry

The factor, U_f, was varied, such that the wind speed at hub height, $U_{10.5}$, ranged from 0 to 0.74 m/s (equation 5). Since this case is not axisymmetric, the two-dimensional system response is studied. The diagnosed areas of influence are shown in Figure 22. Interestingly, upwind sensitivity is much less than downwind sensitivity. Even the slightest ambient wind largely reduces the upwind affected area as compared to the downwind area. The average efficiencies, shown in Figure 23, decreased with increased wind speed. This is a result of slightly lower maximum efficiencies and spatial spreading of the heat (not shown).

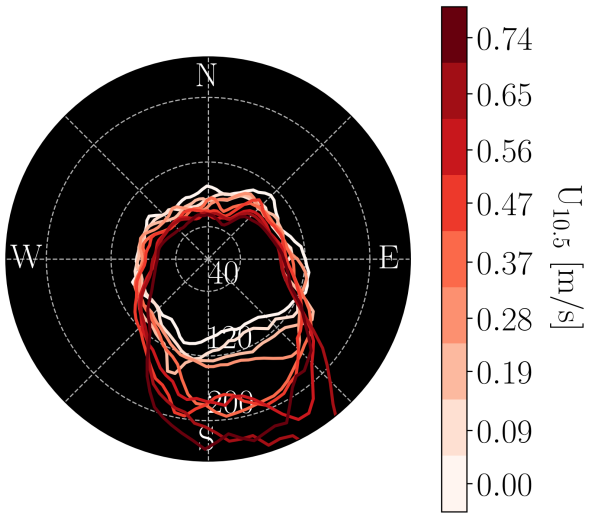

Figure 22: Influence area as a function of fan hub height wind speed, $U_{10.5}$. The wind came from the North.

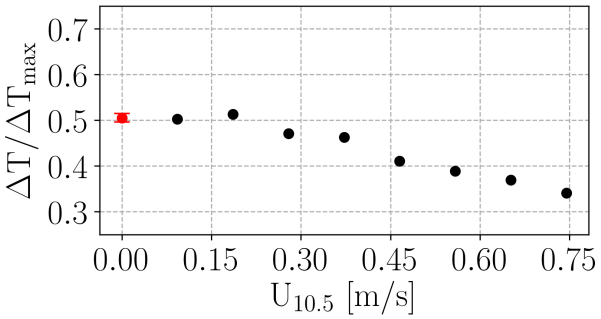

Figure 23: Efficiency as a function of fan hub height wind speed, $U_{10.5}$. Red denotes the five-member ensemble runs.

5.2.5 Inversion strength: temperature, a passive scalar?

For the inversion strength analysis N^2 was varied between 0.1 and 1.6 K/m. The performance measures are shown Figure 24. No significant relation is seen between the influence distance and the inversion strength. However, the efficiency depended strongly on it. This implies that temperature cannot be regarded as a passive scalar: it reduces temperature enhancement even when normalized with the inversion itself. Even more so, with weak inversions, efficiencies tend to 1 so that for weak buoyant forces, temperature behaves like a 'passive scalar' again. Hence, we conclude that generally buoyant forces do play an important role in suppressing transport in the vertical.

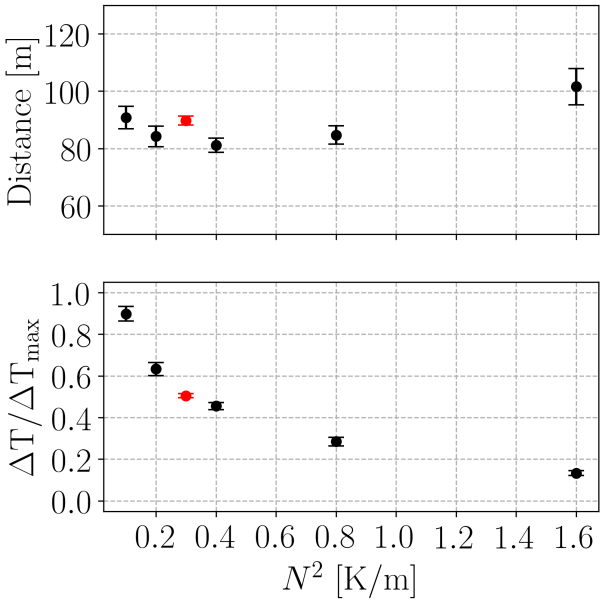

Figure 24: Influence distance and efficiency as a function of N^2. The error bar is an estimate for the variation between runs. Red denotes the five-member ensemble runs.

6 Conclusion

In this study we have employed high-resolution measuring techniques to quantify the local temperature response as a result of wind machine operation. As expected, the observations showed that the actual response strongly depends on the distance to the fan and the height above the surface. In agreement with previous studies, the wind machine was able to achieve rotation-averaged temperature increases up to 50% of the inversion strength (≈3 K) in an area of 3-5 ha. Furthermore, it was observed that low wind speeds (<1 m/s) can cause strong upwind-downwind asymmetries in jet velocity and protected area. Downwind the jet reached further and the affected area was larger as compared to upwind. Finally, it was observed that the engine heat contributes significantly to the local temperature increase. This aspect was given less attention in the past, but could be detected unambiguously with the DTS observations.

In addition to the field experiment, the impact of wind machine operation on the local temperature was studied using turbulence resolving Large Eddy Simulations (LES). It was shown that the spatial temperature response in the simulations was very similar to those observed. A strong asymmetry in the perturbed wind field was found in the simulations in accordance with the outcome of the field experiment. From this it is concluded that the simulations provide a reasonably realistic 'surrogate' for the field experiment in order to do a well-controlled sensitivity study. This to study wind machine performance in response to different forcing parameters.

Performance was expressed in terms of the size of the affected area and temperature enhancement (relative to the background inversion). In essence, the eventual inversion strength is a result of gradient eroding and gradient restoring processes. While, obviously, mixing with warm air from aloft erodes the inversion, it is restored by advection of ambient air, buoyant forces and lateral mixing with cold air within the canopy layer.

Interestingly, it was found that wind machine performance strongly depends on the axial rotation time of the machine. Where temperature enhancement remained relatively constant over different rotation rates (ranging from 3 to 6 minutes), the affected area strongly increased for *slower* rotations! Apparently, one persistent long mixing 'burst' due to slow jet passage, is more beneficial than several short ones. This finding could have important practical consequences and needs to be explored in more depth in the future as to find optimal rotation rates. Note, that a caveat of the present study is that the impact of rotation was studied only for cases without background flow. As such, further exploration is needed in the future to draw definite conclusions.

Investigation of the effect on performance of different tilt angles showed that, in our model, temperature enhancement was maximized between an 8° and 16° tilt angle. Presumably those small angles are very effective in generating strong shear layers which in turn generate Kelvin-Helmholtz type of instabilities. This process increases vertical transport and mixing of heat. Finally, analysis of the sensitivity to the ambient wind speed showed that a strong upwind-downwind asymmetry exists with respect to the affected area. This is in agreement with the findings of our field study.

We believe that future experiments would benefit from similar studies. In particular, experiments in which the size of the horizontal sensor grid is extended and wind data with higher spatial resolution is obtained. Furthermore, multiple vertical profiles could be put in every cardinal direction of the wind machine and measurement distance could be extended in the downwind direction. This will allow for a better understanding of the height varying temperature enhancement, and the asymmetries caused by the ambient wind. From a model perspective, our results can be improved by implementing tree geometries and by using a more realistic description of the prescribed wind and temperature profiles (i.e. non-linear shapes). In view of the authors, it would be both interesting and relevant to extend the philosophy of the present study to other frost mitigation measures at the field scale, so that in the future optimal strategies can be distilled in order to fight frost damage in an effective way.

7 Acknowledgements

We are grateful to Martijn Vogelaar of Fruvo B.V. for providing the experimental site and great practical experience. We also thank Freek van de Wiel, Cynthia Maan, Charlotte Ziedorn, Mariska de Koning and Rene Reudink for their roles in the preparation and deployment of the experimental setup. Maarten Kruis, Jonathan Izett and Steven van der Linden are thanked in particular for their contributions to the former and subsequent discussions. Finally, Erwin de Beurs is thanked for maintaining the local computational cluster on which simulations ran.

A Experimental background

A.1 Influence of the Oosterschelde

To study the influence of the Oosterschelde, a high-resolution forecast of the study area was done using the GRASP LES model on a GPU machine by weather research company Whiffle (`www.whiffle.nl`, Schalkwijk et al. (2015)). The LES was externally forced by data from the numerical weather prediction model ECMWF for January 20, 2019. One case was run with high and one with low tide. The average wind speed slices at 3 m height during wind machine operation are shown in Figure 25 for both cases.

Significant differences are seen both in wind speed and direction. The presence of relatively warm and rough water decreases the stability and thus favors momentum transport towards the surface. This implies that radiation frost events are less likely to occur during high tide than during low tide.

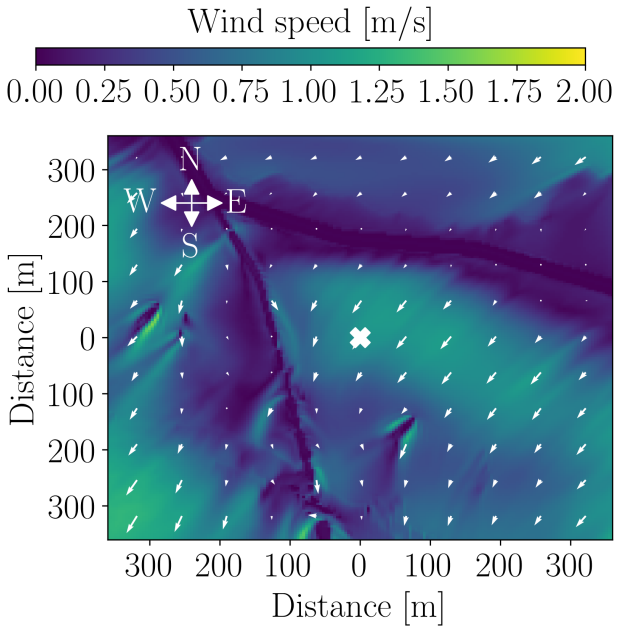

(a) Low tide

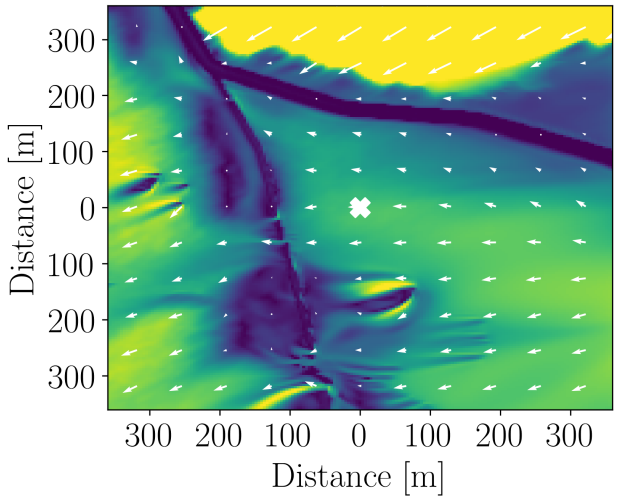

(b) High tide

Figure 25: Average 3 m wind speed during the experiment using a high-resolution forecast, comparing low and high tide. The cross denotes the position of the fan and the arrows indicate the wind vector.

A.2 Soil cover

Figure 26: Alternating soil cover of litter under the trees and grass between the rows. The 1 m and 0 m West-East cables are also visible.

A.3 Data fitting parameters

The full range of fitted parameters to the experimental data are shown in table 2. Please note that negative covariances can result in lower fitting uncertainties in measures consisting of multiple parameters (i.e. Distance and Max Efficiency).

Table 2: Fitting parameters to the experimental data. Fitting uncertainties smaller then the least significant digit are not shown.

Section	a	b [m]	c [m]	d
South 1 m	0.5	40.0 ± 0.5	43.9 ± 0.4	0.0
West 1 m	0.53 ± 0.89	23.5 ± 3.0	81.2 ± 78.3	± 0.9
East 1 m	0.37 ± 0.02	29.6 ± 1.1	38.2 ± 2.0	± 0.02
West 0 m	0.53 ± 0.4	14.3 ± 6.7	62.3 ± 35.0	± 0.4
East 0 m	0.44 ± 0.01	27.0 ± 1.0	24.4 ± 1.1	± 0.01

B Simulation background

B.1 Wind machine implementation

The implementation is based on a momentum forcing. An amount of work per time is done on the flow with a certain power, P. Using the work-energy theorem, which states that the work done by all acting forces on a particle is equal the change in kinetic energy, this can be expressed as $\Delta \mathrm{E_{kin}} = \mathrm{P}\Delta t$. This directly implies that,

$$\vec{v}_{t+\Delta t}^2 - \vec{v}_t^2 = \frac{2\mathrm{P}\Delta t}{m}\hat{n}^2 \tag{8}$$

which in turn implies for every spatial dimension,

$$v_{i,t+\Delta t}^2 - v_{i,t}^2 = \frac{2\mathrm{P}\Delta t}{m}n_i^2 \tag{9}$$

From these equations the direction of $\hat{n}$ is not yet defined and $|\hat{n}| = 1$. When it is assumed that the force applied to the flow is normal to the plane in which the fan blades rotate then $\hat{n}$ is the normal vector of this plane. Rearranging equation 9 and taking the square root results in,

$$\vec{v}_{i,t+\Delta t} = \sqrt{\vec{v}_{i,t}^2 + \frac{2\mathrm{P}\Delta t}{m}\hat{n}_i^2} \tag{10}$$

For the numerical implementation see: `http://basilisk.fr/sandbox/vheusinkveld/fan.c`.

To estimate the velocity to which air is accelerated by this forcing we assume that it is applied over a finite time from t_{start} to t_{end}, moving a distance w in the process:

$$w = \int_{t_{start}}^{t_{end}} v\,(t)\,\mathrm{dt} \tag{11}$$

Assuming a zero entrance velocity, v is given at every instance as:

$$\begin{aligned} \mathrm{E_{kin}} &= \mathrm{P}\Delta t = 0.5mv^2 \\ v\,(t) &= \sqrt{2\mathrm{P}t/m} \end{aligned} \tag{12}$$

P, w and m are set by the user. This leaves two equations and two unknowns. Solving for the exit velocity results in:

$$v_{end} = \left(\frac{3\mathrm{P}w}{m}\right)^{1/3} \tag{13}$$

References

Earl M. Bates, Porter B. Lombard, et al. Evaluation of temperature inversions and wind machine on frost protection in southern oregon. Technical report, Oregon State University. Agricultural Experiment Station, 1978.

John B Bell, Phillip Colella, and Harland M Glaz. A second-order projection method for the incompressible navier-stokes equations. *Journal of Computational Physics*, 85(2):257–283, dec 1989. doi: 10.1016/0021-9991(89)90151-4.

G Berz. Losses in the range of us $50 billion and 50 000 people killed: Munich re's list of major natural disasters in 1990. *Natural hazards*, 5(1):95–102, 1992.

Víctor Beyá-Marshall, Julio Herrera, Fernando Santibáñez, and Thomas Fichet. Microclimate modification under the effect of stationary and portable wind machines. *Agricultural and Forest Meteorology*, 269-270:351 – 363, 2019. ISSN 0168-1923. doi: https://doi.org/10.1016/j.agrformet.2019.01.042.

S. Boing, H. J. J. Jonker, B. J. H. van de Wiel, and A. F. Moene. Intermittent turbulence in stratified flow over a canopy. Extended Abstracts, 19th Symp. on Boundary Layers and Turbulence, Keystone, CO, Amer. Meteor. Soc., 7.2. Available online at `http://ams.confex.com/ams/pdfpapers/172716.pdf`., 2010.

Achi Brandt. Multi-level adaptive solutions to boundary-value problems. *Mathematics of computation*, 31(138): 333–390, 1977.

F. Brooks, D. Rhoades, A. Leonard, et al. Wind machine tests in citrus: Frost protection studies in 1954 confirmed earlier findings next to be investigated in deciduous trees. *California Agriculture*, 8(8):8–10, 1954.

Andrés Alonso Castillo-Castellanos. *Turbulent convection in Rayleigh-Bénard cells with modified boundary conditions*. PhD thesis, Université Pierre et Marie Curie, 2017.

Robert G Evans. Frost protection in orchards and vineyards. *Washington State Univ. Coop. Ext. Pullman*, 1999.

John J. Finnigan, Roger H. Shaw, and Edward G. Patton. Turbulence structure above a vegetation canopy. *Journal of Fluid Mechanics*, 637:387–424, 2009. doi: 10.1017/S0022112009990589.

Google Maps. XYZ tile server. Krabbendijke, 51°25′44.7″N, 4°8′8.5″E. URL `http://mt0.google.com/vt/lyrs=s&hl=en&x={x}&y={y}&z={z}`. Retrieved on: 2019-01-18.

Jetse D. Kalma, Gregory P. Laughlin, Joseph M. Caprio, and Paul J. C. Hamer. *The Bioclimatology of Frost: Its Occurrence, Impact and Protection*, volume 2 of *Advances in Bioclimatology*. Springer, 1992. ISBN 3-540-53855-0.

Stéphane Popinet. An accurate adaptive solver for surface-tension-driven interfacial flows. *Journal of Computational Physics*, 228(16):5838–5866, sep 2009. doi: 10.1016/j.jcp.2009.04.042.

Stéphane Popinet. A quadtree-adaptive multigrid solver for the serre–green–naghdi equations. *Journal of Computational Physics*, 302:336–358, dec 2015. doi: 10.1016/j.jcp.2015.09.009.

António C. Ribeiro, J. Paulo De Melo-Abreu, and Richard L. Snyder. Apple orchard frost protection with wind machine operation. *Agricultural and Forest Meteorology*, 141(2-4):71–81, dec 2006. doi: 10.1016/j.agrformet.2006.08.019.

Jerôme Schalkwijk, Harmen JJ Jonker, A Pier Siebesma, and Erik Van Meijgaard. Weather forecasting using gpu-based large-eddy simulations. *Bulletin of the American Meteorological Society*, 96(5):715–723, 2015.

M. Scharringa. *Nachtvorst*. KNMI, Verspreide opstellen no. 5. 's-Gravenhage: Staatsdrukkerij, 1962.

John S. Selker, Luc Thévenaz, Hendrik Huwald, Alfred Mallet, Wim Luxemburg, Nick van de Giesen, Martin Stejskal, Josef Zeman, Martijn Westhoff, and Marc B. Parlange. Distributed fiber-optic temperature sensing for hydrologic systems. *Water Resources Research*, 42(12), dec 2006. doi: 10.1029/2006wr005326.

Sillixa Ltd. *Ultima DTS Datasheet 2018*. Sillixa Ltd. URL `https://silixa.com/wp-content/uploads/DTS-datasheet-2018.pdf`.

James J. Smolen and Alex van der Spek. *Distributed Temperature Sensing: A DTS Primer for Oil & Gas Production*. Shell, 2003.

Richard L. Snyder and J. Paulo de Melo-Abreu. *Frost Protection: fundamentals, practice, and economics*, volume 1. Food and Agriculture Organization of the United Nations, 2005. ISBN 92-5-105328-6.

Bas Des Tombe and Bart Schilperoort. dtscalibration/python-dts-calibration: v0.6.4, 2019.

Bas J. H. van de Wiel, Etienne Vignon, Peter Baas, Ivo G. S. van Hooijdonk, Steven J. A. van der Linden, J. Antoon van Hooft, Fred C. Bosveld, Stefan R. de Roode, Arnold F. Moene, and Christophe Genthon. Regime transitions in near-surface temperature inversions: A conceptual model. *Journal of the Atmospheric Sciences*, 74(4): 1057–1073, apr 2017. doi: 10.1175/jas-d-16-0180.1.

J. Antoon van Hooft, Stéphane Popinet, and Bas J. H. van de Wiel. Adaptive cartesian meshes for atmospheric single-column models, a study using basilisk 18-02-16. *Geoscientific Model Development Discussions*, pages 1–14, March 2018a. doi: 10.5194/gmd-2018-21.

J. Antoon van Hooft, Stéphane Popinet, Chiel C. van Heerwaarden, Steven J. A. van der Linden, Stephan R. de Roode, and Bas J. H. van de Wiel. Towards adaptive grids for atmospheric boundary-layer simulations. *Boundary-Layer Meteorology*, 167(3):421–443, February 2018b. doi: 10.1007/s10546-018-0335-9.

J. Antoon van Hooft, Peter Baas, Maurice van Tiggelen, Cedrick Ansorge, and Bas J. H. van de Wiel. An idealized description for the diurnal cycle oft he dry atmospheric boundary layer. *Submitted to Journal of the Atmospheric Sciences*, 2019.

AW Vreman. An eddy-viscosity subgrid-scale model for turbulent shear flow: Algebraic theory and applications. *Physics of fluids*, 16(10):3670–3681, 2004.

Gilbert F White and John Eugene Haas. *Assessment of research on natural hazards*. Massachusetts Institute of Technology Press, 1975.

John C. Wyngaard. *Turbulence in the Atmostphere*. Cambridge University Press, 2010. ISBN 9780521887694.

Matthias J. Zeeman, John S. Selker, and Christoph K. Thomas. Near-surface motion in the nocturnal, stable boundary layer observed with fibre-optic distributed temperature sensing. *Boundary-Layer Meteorology*, 154(2): 189–205, oct 2014. doi: 10.1007/s10546-014-9972-9.